Water Production and Release in Comet C/1995 O1 Hale–Bopp

Neil Dello Russo

Department of Physics, The Catholic University of America, Washington, DC 20064 & Laboratory for Extraterrestrial Physics,
NASA Goddard Space Flight Center Code 690.2, Greenbelt, Maryland 20771
E-mail: ysndr@lepvax.gsfc.nasa.gov

Michael J. Mumma

Laboratory for Extraterrestrial Physics, NASA Goddard Space Flight Center Code 690, Greenbelt, Maryland 20771

Michael A. DiSanti

Department of Physics, The Catholic University of America, Washington, DC 20064, and Laboratory for Extraterrestrial Physics,
NASA Goddard Space Flight Center Code 690.2, Greenbelt, Maryland 20771

and

Karen Magee-Sauer, Robert Novak, and Terrence W. Rettig

Department of Chemistry and Physics, Rowan University, Glassboro, New Jersey 08028; Department of Physics, Iona College, New Rochelle,
New York 10801; and Department of Physics and Astronomy, University of Notre Dame, Notre Dame, Indiana 46556

Water (H_2O) was detected in Comet C/1995 O1 Hale–Bopp on 10 dates between UT January 21.8 and May 1.2, 1997, using high-resolution infrared spectroscopy. This is the first study of the heliocentric dependence of water released from a comet using direct detection of H_2O itself. Production rates and rotational temperatures were measured, and the derived heliocentric dependence for the water production rate is $Q = (8.35 \pm 0.13) \times 10^{30} [R_h^{(-1.88 \pm 0.18)}]$ molecules s^{-1}. The spatial distribution of H_2O molecules in the coma is consistent with water being released directly from the nucleus within 1.5 AU of the Sun, although release of a small fraction from icy grains cannot be excluded. When our derived water production rates are compared to the production of native carbon monoxide and dust, we obtain a dust to ice mass ratio of 5.1 ± 1.2 within a heliocentric distance of 1.5 AU. The abundance of H_2O provides a benchmark for the volatile inventory in Hale–Bopp and, when compared to interstellar and nebular material, helps constrain the origin of cometary ices and their processing histories. These production rates derived from the direct detection of H_2O provide a sound basis with which water production rates inferred by indirect methods can be compared. © 2000 Academic Press

Key Words: comets; Hale–Bopp; composition; infrared observations; water.

1. INTRODUCTION

The cometary nucleus contains a mixture of volatile ices and refractory grains which are thought to date from (or to predate) the formative phase of our Solar System. Since that epoch, material within the nucleus has been shielded in a low-temperature environment and by an overburden of surface material. Thus, the composition of comets may reflect physical and chemical conditions in the early Solar System. Since the degree of processing experienced by ices prior to incorporation into the nucleus constrains physical conditions in the region of comet formation, the nature of the nucleus is the central problem in cometary science.

The manner in which volatile species are released from the nucleus provides information on the physical nature of cometary material. Volatile species contained as ice within the nucleus are termed "native," and are said to have a "direct" source when sublimed from the nucleus itself. Species released in the coma—whether from grains (dust or ice), as photodissociation products of parent volatiles, or by active coma chemistry—are said to have a "distributed" source. It is possible for a native species to show a distributed source if released from icy grains dragged into the coma. Some volatile species (e.g., CO) exhibit both direct and distributed sources (Eberhardt *et al.* 1987, Greenberg and Li 1998, DiSanti *et al.* 1999). Under favorable circumstances, the number, nature, and relative abundances of sources for a given volatile species can be inferred from its spatial distribution about the nucleus. However, the spatial distribution of water (H_2O) in the cometary coma has not been directly studied, except along the paths of spacecraft threading the coma of Comet 1P/Halley (cf. Combes *et al.* 1988).

In its current view, the icy conglomerate nucleus consists of numerous exotic ices and dust (Whipple 1950). Water is the dominant ice in most (perhaps all) comets and its sublimation controls the release of other volatiles within 3–4 AU of the Sun. For this reason, the volatile activity of a comet and the abundances of minor species are often expressed relative to H_2O production (molecules s^{-1}). At greater distances, more volatile species such as CO may control a comet's activity (Senay and Jewitt 1994, Crovisier *et al.* 1995), and water is likely released primarily from a distributed source of icy grains. Despite its key importance, direct detection of cometary water from the ground has been problematic due to atmospheric extinction. This has hampered studies of water production and limited our understanding of the manner in which water is released from comets.

The early discovery of the bright Comet C/1995 O1 Hale–Bopp provided an opportunity to track cometary activity as a function of heliocentric distance and to study the nature of water release. Soon after its discovery, water production rates in Hale–Bopp were inferred from radio and ultraviolet observations of OH beginning at a heliocentric distance of 7.4 AU (Biver *et al.* 1997a, Schleicher *et al.* 1997, Weaver *et al.* 1997a). Water ice absorption was first detected at 7 AU (Davies *et al.* 1997), and emission from water vapor (in the ν_3 vibrational fundamental band at 2.7 μm) was measured at 2.9 AU with the Infrared Space Observatory (Crovisier *et al.* 1997).

Here, we report a comprehensive study of water release in Comet Hale–Bopp, based on direct groundbased detection of water emission lines using high-resolution infrared spectroscopy. Production rates, rotational temperatures, and spatial distributions for water in Comet Hale–Bopp were measured as a function of heliocentric distance within 1.5 AU of the Sun. Our measurements provide a benchmark with which water production rates inferred from indirect methods can be compared. The high spectral and spatial resolution of our measurements helps reveal the connection between the distribution of water vapor in the coma and water ice present in the nucleus. Our analysis shows that most water was released directly from the nucleus for heliocentric distances (R_h) < 1.5 AU.

2. BACKGROUND

Water production rates in comets have traditionally been inferred through detection of its photodissociation products OH (at near-ultraviolet and radio frequencies; cf. Schleicher and A'Hearn 1982, Tacconi-Garman *et al.* 1990), O (through ^1D emission in the visible; cf. Fink and Hicks 1996), and H (through H Ly-α emission; cf. Combi *et al.* 1998). However, these can be produced from other parents, and all indirect methods require modeling assumptions to relate the production of the measured species to that of water. Although detection of vibrational and rotational emission from water vapor in comets is possible at high altitudes (Mumma *et al.* 1986) and from space (Combes *et al.* 1988, Crovisier *et al.* 1997), airborne observatories present

limited observing opportunities and space observatories have limited lifetimes and Sun-avoidance constraints. For these reasons, we developed a general method for detection of water from groundbased observatories and applied it to Comet Hale–Bopp.

Severe extinction by atmospheric water makes direct detection of water in comets difficult from groundbased observatories—its strong transitions terminate in the ground vibrational level which is highly populated in Earth's atmosphere, causing absorption of the incident photons. To avoid such extinction, we target water lines in nonresonance fluorescence—direct absorption of sunlight excites molecules from the lowest vibrational level (000) to a higher vibrational level, followed by cascade into an intermediate level which is not significantly populated in the atmosphere (see Appendix). The terrestrial atmosphere is generally transparent to these cometary water emissions, and no specific Doppler shift is needed to observe these "hot-band" lines. This strategy can be extended to groundbased infrared observations of other cold objects, for example planetary atmospheres and preplanetary disks around young stars.

With this approach, water was securely detected in Comets C/1991 T2 Shoemaker–Levy, 6P/d'Arrest, and C/1996 B2 Hyakutake using the $\nu_1+\nu_2+\nu_3-\nu_1$ (111–100) vibrational band near 2 μm (Mumma *et al.* 1995, 1996). Production rates were obtained for all three comets, and a rotational temperature was obtained for H_2O in Comet Hyakutake (Mumma *et al.* 1996). Our survey of the (1–0) band of CO at $\sim$4.7 μm in Hyakutake unexpectedly revealed new strong emissions which were identified as nonresonance fluorescence from the $\nu_1-\nu_2$ (100–010) and $\nu_3-\nu_2$ (001–010) hot bands of H_2O. We later realized that the possibility of observing these two bands in comets had been considered previously (Bockelée-Morvan and Crovisier 1989). We targeted lines from these three hot bands in Comet Hale–Bopp.

3. OBSERVATIONS AND DATA ANALYSIS

Ro-vibrational lines from these three hot bands were detected on ten separate dates between UT Jan. 21.8 (R_h = 1.48 AU preperihelion) and UT May 1.2, 1997 (R_h = 1.06 AU postperihelion) in Comet Hale–Bopp (Table I). Water was searched for on UT Aug. 8.0, 1997 (R_h = 2.24 AU), and an upper limit was determined. We used the cryogenic echelle spectrometer (CSHELL) at the NASA Infrared Telescope Facility on Mauna Kea, Hawaii (Greene *et al.* 1993). CSHELL has a 256 × 256-pixel InSb array detector with a pixel size of 0.2 arcsec and provides spatial coverage along the 30-arcsec-long slit which we oriented east–west. A 1-arcsec-wide slit was used for our comet observations leading to a spectral resolving power $\nu/\Delta\nu \sim 2 \times 10^4$. At each grating setting, cometary data were acquired using a sequence of four scans (source, sky, sky, source), with an integration time of 2 min on source per sequence of scans. Sky

TABLE I
Water Lines Detected in Comet Hale–Bopp

Band assignment	Line assignment	Rest frequency (cm^{-1})	g Factors ($\times 10^{-7}$) s^{-1}[a]	Date(s) detected (UT 1997)
111–100	2_{02}–3_{03}	5083.94	0.20 (60 K) 0.17 (80 K) 0.14 (100 K) 0.12 (120 K)	Feb 24.0, Apr 30.0
001–010	0_{00}–1_{01}	2137.37	8.22 (60 K) 6.28 (80 K) 4.94 (100 K) 4.01 (120 K)	Jan 21.8, Mar 1.9
001–010	1_{11}–1_{10}	2151.19	5.70 (60 K) 5.22 (80 K) 4.61 (100 K) 4.05 (120 K)	Jan 21.8, Mar 1.9, Apr 16.0, Apr 30.0, May 1.2
100–010	0_{00}–1_{11}	2022.08	1.82 (60 K) 1.40 (80 K) 1.12 (100 K) 0.90 (120 K)	Apr 9.0, Apr 16.0, Apr 30.0, May 1.2
100–010	1_{01}–1_{10}	2039.95	7.15 (60 K) 5.91 (80 K) 4.94 (100 K) 4.16 (120 K)	Jan 21.8, Feb 24.0, Mar 1.9, Apr 8.1, Apr 9.0, Apr 16.0, Apr 30.0, May 1.2
100–010	1_{01}–2_{12}	2003.39	6.10 (60 K) 5.04 (80 K) 4.21 (100 K) 3.55 (120 K)	Jan 21.8, Mar 1.9, Apr 6.2, Apr 9.0, Apr 10.2, Apr 16.0, Apr 30.0, May 1.2
100–010	1_{11}–2_{02}	2028.32	0.70 (60 K) 0.58 (80 K) 0.49 (100 K) 0.43 (120 K)	Apr 16.0, May 1.2
100–010	2_{02}–2_{11}	2032.29	1.66 (60 K) 1.48 (80 K) 1.32 (100 K) 1.18 (120 K)	Apr 16.0, May 1.2
100–010	2_{12}–3_{03}	2003.00	2.59 (60 K) 2.43 (80 K) 2.24 (100 K) 2.03 (120 K)	Mar 1.9, Apr 6.2, Apr 9.0, Apr 10.2, Apr 16.0, Apr 30.0, May 1.2
100–010	2_{21}–1_{10}	2148.19	1.24 (60 K) 1.37 (80 K) 1.43 (100 K) 1.44 (120 K)	Jan 21.8, Apr 9.0, Apr 10.2, Apr 16.0, Apr 30.0, May 1.2
100–010	2_{21}–3_{30}	1881.08	1.42 (60 K) 1.57 (80 K) 1.64 (100 K) 1.64 (120 K)	Apr 16.0, May 1.2

[a] For $R_h = 1$ AU and an ortho to para ratio of 3.

spectra were obtained by nodding the telescope 2 arcmin from the source, providing sky cancellation via pixel-by-pixel subtraction (source–sky–sky+source). Flat-fields and dark frames were obtained immediately following each scan sequence. For each grating setting, spectra of infrared standard stars were obtained through a 4-arcsec-wide slit for absolute flux calibration of the comet spectra (Table II).

Most observations occurred during daylight when atmospheric seeing is generally poorer and more variable and tracking is more difficult (since the autoguiding capability of the telescope

TABLE II
Derived Line Fluxes and Production Rates for Water Lines in Comet Hale–Bopp

Date UT 1997	Infrared flux standard stars[a]	Vibrational line assignment	Rotational line assignment[b]	Line flux (10^{-17} W m^{-2}) on the nucleus[c]	Line flux (10^{-16} W m^{-2}) off the nucleus[d]	Q_{H_2O} (10^{30} molec s^{-1})[e]
Jan 21.8	BS 6707 (ν Her)	001–010	$1_{11}-1_{10}$	0.79 ± 0.11	0.424 ± 0.054	3.49 ± 0.84
		001–010	$1_{11}-1_{10}$	0.68 ± 0.10	0.532 ± 0.045	4.38 ± 0.72
		001–010	$0_{00}-1_{01}$	1.24 ± 0.13	0.644 ± 0.066	4.31 ± 0.82
		001–010	$0_{00}-1_{01}$	1.35 ± 0.12	0.562 ± 0.054	3.76 ± 0.71
		100–010	$1_{01}-1_{10}$	1.87 ± 0.25	0.67 ± 0.12	5.0 ± 1.6
Feb 24.0	BS 1165 (η Tau)	100–010	$1_{01}-1_{10}$	4.82 ± 0.17	2.38 ± 0.08	8.89 ± 0.89
		111–100	$2_{02}-3_{03}$	0.54 ± 0.06	0.20 ± 0.05	10.3 ± 4.3
Mar 1.9	BS 6707	001–010	$1_{11}-1_{10}$	4.82 ± 0.10	2.03 ± 0.05	7.38 ± 0.37
		001–010	$0_{00}-1_{01}$	4.44 ± 0.10	2.35 ± 0.05	7.38 ± 0.37
		100–010	$1_{01}-2_{12}$	4.49 ± 0.18	2.03 ± 0.08	8.24 ± 0.61
		100–010	$1_{01}-1_{10}$	5.52 ± 0.16	2.32 ± 0.07	7.91 ± 0.47
		100–010	$1_{01}-1_{10}$	5.99 ± 0.24	2.34 ± 0.11	7.98 ± 0.71
		100–010	$0_{00}-1_{11}$	2.21 ± 0.23	0.54 ± 0.11	8.0 ± 2.5
Apr 6.2	BS 2560 (15 Lyn)	100–010	$1_{01}-2_{12}$	7.05 ± 0.09	2.93 ± 0.04	10.69 ± 1.07
Apr 8.1	BS 2560	100–010	$1_{01}-1_{10}$	5.55 ± 0.21	3.00 ± 0.08	9.34 ± 0.93
Apr 9.0	BS 2560	100–010	$1_{01}-2_{12}$	4.38 ± 0.13	2.33 ± 0.06	8.84 ± 0.88
		100–010	$1_{01}-2_{12}$	4.33 ± 0.14	2.51 ± 0.06	9.50 ± 0.95
		100–010	$1_{01}-1_{10}$	5.15 ± 0.20	3.08 ± 0.08	9.75 ± 0.98
		100–010	$0_{00}-1_{11}$	2.10 ± 0.17	0.96 ± 0.08	13.5 ± 2.9
Apr 10.2	BS 2560	100–010	$2_{21}-1_{10}$	2.42 ± 0.09	1.00 ± 0.033	10.59 ± 0.71
		100–010	$2_{21}-1_{10}$	1.49 ± 0.08	0.885 ± 0.035	9.35 ± 0.74
		100–010	$1_{01}-2_{12}$	5.93 ± 0.09	2.62 ± 0.04	9.99 ± 0.50
Apr 16.0	BS 2560	100–010	$2_{21}-1_{10}$	1.63 ± 0.09	0.827 ± 0.042	9.75 ± 1.74
		100–010	$2_{21}-1_{10}$	2.08 ± 0.08	0.751 ± 0.036	8.85 ± 1.30
		100–010	$1_{01}-2_{12}$	6.00 ± 0.12	2.38 ± 0.05	9.36 ± 0.47
		100–010	$1_{01}-1_{10}$	5.43 ± 0.19	2.67 ± 0.08	8.80 ± 0.55
		100–010	$2_{21}-3_{30}$	3.51 ± 0.17	1.05 ± 0.08	12.30 ± 1.60
Apr 30.0	BS 8781 (α Peg)	100–010	$2_{21}-1_{10}$	2.29 ± 0.14	0.436 ± 0.062	7.10 ± 1.14
		100–010	$2_{21}-1_{10}$	2.08 ± 0.16	0.393 ± 0.049	6.40 ± 1.04
		100–010	$1_{01}-2_{12}$	2.75 ± 0.13	1.46 ± 0.06	6.64 ± 0.49
		100–010	$1_{01}-2_{12}$	4.13 ± 0.18	1.66 ± 0.08	7.52 ± 0.69
		100–010	$1_{01}-1_{10}$	5.61 ± 0.15	1.71 ± 0.07	6.49 ± 0.50
		100–010	$0_{00}-1_{11}$	2.12 ± 0.19	0.76 ± 0.08	12.2 ± 2.3
		111–100	$2_{02}-3_{03}$	0.44 ± 0.13	0.16 ± 0.03	9.0 ± 2.9
May 1.2	BS 8781	100–010	$2_{21}-1_{10}$	2.54 ± 0.10	0.448 ± 0.046	7.39 ± 0.94
		100–010	$1_{01}-2_{12}$	3.50 ± 0.13	1.59 ± 0.58	7.64 ± 0.54
		100–010	$1_{01}-1_{10}$	4.48 ± 0.16	1.79 ± 0.67	7.21 ± 0.56
		100–010	$0_{00}-1_{11}$	1.31 ± 0.14	0.51 ± 0.07	8.7 ± 2.4
		100–010	$2_{21}-3_{30}$	1.43 ± 0.17	0.49 ± 0.08	8.1 ± 2.4
		100–010	$2_{02}-2_{11}$	1.28 ± 0.11	0.45 ± 0.05	7.3 ± 1.2
		100–010	$1_{11}-2_{02}$	0.72 ± 0.10	0.18 ± 0.04	7.5 ± 2.8
Aug 8.0	BS 1165	100–010	$1_{01}-2_{12}$	<0.024		$<1.5^{f}$

[a] BS numbers are given with the star name in parentheses. The same calibration star was used for each grating setting on a particular date.

[b] Lines repeated in the table indicate separate measurements.

[c] Transmittance-corrected flux in a 1×1 arcsec box centered on the nucleus.

[d] Total transmittance-corrected flux 2–12 arcsec off the nucleus in both the east and west direction.

[e] A quantitative analysis was not done for some detected lines: Some lines were too weak, fell in regions of low atmospheric transmittance, or were blended with emissions from other species.

[f] A 3σ upper limit derived from the measured upper limit for the flux on the nucleus and assuming it to be low by a factor of 3 due to seeing, cometary drift, etc.

is not usable) compared to night-time observations. Images of the comet were taken before and after each sequence of scans through a circular variable filter at $3.5\,\mu$m to assess cometary drift and to update telescope tracking rates as needed. Defocusing can occur if sunlight strikes the telescope structure, so focus was also checked and updated regularly using a star close to the comet. All these factors (and other unrecognized ones) which result in what we term "nonideal" observing conditions, affect the measured point-spread function (PSF) of an object. For our observations, the full width at half maximum (FWHM) of a stellar PSF was typically ~1–2 arcsec and was generally variable within a single date.

The data were processed using algorithms specifically tailored to our comet observations. Initial processing included flat-fielding, removal of high dark current pixels and cosmic ray hits, and registration of spectral frames such that the spectral dimension falls along a row and the spatial dimension is orthogonal to this (Fig. 1A). Spectra were extracted over any desired spatial extent and position along the slit; an example is shown in Fig. 1B. Atmospheric models were obtained using the Spectrum Synthesis Program (SSP) (Kunde and Maguire 1974) which accesses the HITRAN-1992 Molecular Data Base (Rothman *et al.* 1992). SSP models were used to assign wavelength scales to the extracted spectra and to establish absolute column burdens for the component absorbing species in the terrestrial atmosphere. The model was convolved to the resolution of the comet spectrum, binned to the instrumental sampling interval, and normalized to the cometary continuum (Fig. 1B).

Two water emissions in Comet Hale–Bopp are shown in Fig. 1. The signal-to-noise ratio in the cometary water lines was very high, but the prodigious dust production (high thermal continuum emission) in Hale–Bopp caused the line-to-continuum contrast to be low (Figs. 1A and 1B). Line visibility was enhanced by scaled (row-by-row) subtraction of the optimized transmittance model from the comet spectrum, yielding the net cometary molecular emissions (Fig. 1C) still convolved with the atmospheric transmittance function. The true line flux incident at the top of the terrestrial atmosphere was obtained from the observed line flux by correcting for the monochromatic transmittance obtained from the fully resolved SSP model at the Doppler-shifted line position.

4. THE SPATIAL DISTRIBUTION OF WATER IN THE COMA

The high spectral and spatial resolution afforded by CSHELL provided a unique opportunity to measure and compare the spatial distribution of H_2O with that of other volatiles and dust in the coma of Comet Hale–Bopp. The distribution of a species in the coma (along the slit, in our case) is termed its spatial profile (Fig. 2). The manner in which a species is released from the nucleus affects the general shape of its profile: In the absence of decay (e.g., photodissociation), the column density for a species released solely from the nucleus and with spherical symmetry (at a constant rate and expanding with uniform outflow velocity)

falls off as ρ^{-1} (where ρ is the projected distance from the nucleus). The spatial profile for a species with a distributed source contribution will be broader, falling off more slowly than ρ^{-1}. However, properties of the comet and observing conditions also affect profile shapes, causing deviations from a ρ^{-1} distribution. Nonideal observing conditions will always contribute to departures from ρ^{-1} close to the nucleus (flattening and broadening the profiles), and they will affect the spatial profiles of species released from the nucleus (volatiles and dust) in similar ways when measured simultaneously (in the same exposure). Farther from the nucleus, small departures from ρ^{-1} are also seen due to the variable nature of comets (e.g., outflow asymmetries and jet activity), and this may affect the spatial profiles of species differently. Therefore, a distribution somewhat broader than ρ^{-1} is typically seen even in the absence of a distributed source.

Can distributed source contributions be separated from competing effects which cause deviations from ρ^{-1}? Spatial profiles for CO near perihelion show pronounced deviations from ρ^{-1} out to ~5 arcsec from the nucleus, which cannot be explained solely by nonideal observing conditions or outflow variability (cf. Fig 2B). In fact, about one-half of the total CO released from Hale–Bopp is contributed by a distributed source, for heliocentric distances within 1.5 AU (DiSanti *et al.* 1999). However, detecting small distributed source contributions close to the nucleus is difficult since spatial information in this region is distorted by nonideal observing conditions. The extent of the region influenced by nonideal observing conditions is represented within the FWHM of a stellar PSF (assuming observing conditions were similar for the comet and star). Thus, spatial profiles can provide a qualitative means for detecting significant distributed source contributions, but are unreliable for determining contributions from small distributed sources close to the nucleus.

Spatial profiles for water and dust show small asymmetries (Fig. 2A), but they fall off as approximately ρ^{-1} (beyond ~1–2 arcsec from the nucleus) for all heliocentric distances less than 1.5 AU. This behavior is consistent with release of both directly from the nucleus, or within ~1–2 arcsec (~1000–2000 km) of the nucleus, although small distributed source contributions within this region cannot be ruled out. An analysis from independent CSHELL observations on UT March 5 (R_h ~ 1.03 AU) is also consistent with most water being released directly from the nucleus (Weaver *et al.* 1997b).

5. ROTATIONAL TEMPERATURES

Knowledge of the rotational temperature is needed to determine total production rates from individual line intensities. A rotational temperature can be inferred from the relative intensities of observed water lines, which are proportional to the temperature-dependent g factors for these lines. The method for calculating g factors is discussed in the Appendix. We determine the temperature in the excited vibrational level from the
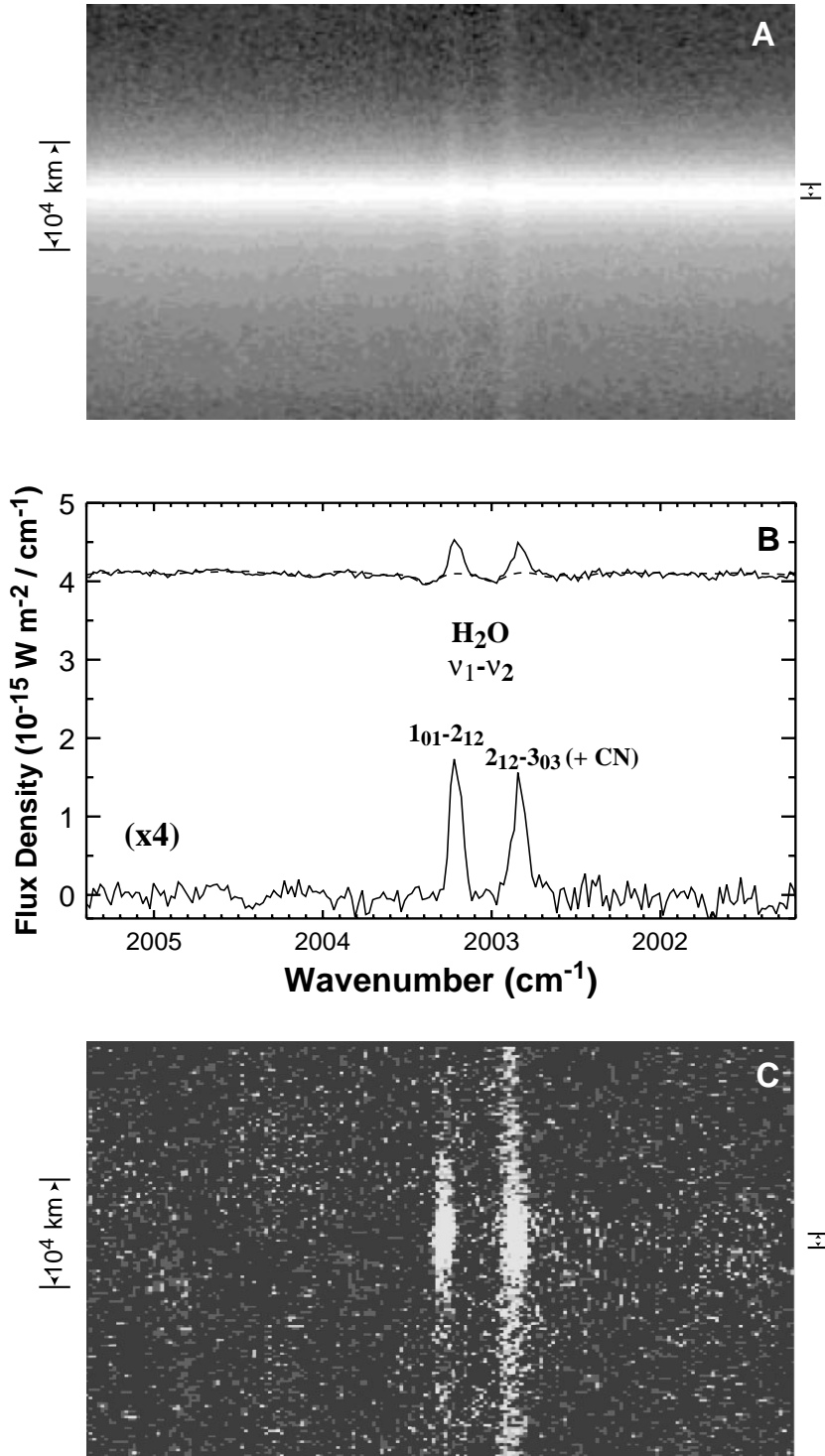
FIG. 1. Detection of H_2O in Comet Hale–Bopp on UT May 1.2, 1997. (A) On-chip spatial–spectral image showing molecular emissions and the dust continuum. The spatial dimension is along columns and the spectral dimension is along rows. The spatial extent of the image is ∼30 arcsec on the sky, with a spatial scale of ∼260 km pixel^{-1} at the comet. East is at the top. (B) Extracted cometary spectrum (solid line). The spatial extent of the extracted spectrum is 1 arcsec (5 rows) and is represented by arrows to the right of A and C. Subtraction of an optimized atmospheric model spectrum (dashed line) reveals cometary water emissions in the residuals (expanded vertically by a factor of 4). (C) The spectral image shown in A after removal of the dust continuum via row-by-row scaled subtraction of the atmospheric model. Continuum subtraction clearly shows the spatial extent of the water emissions, and reveals a distributed CN emission located ∼0.03 cm^{-1} to the blue of the 2_{12}–3_{03} water line.
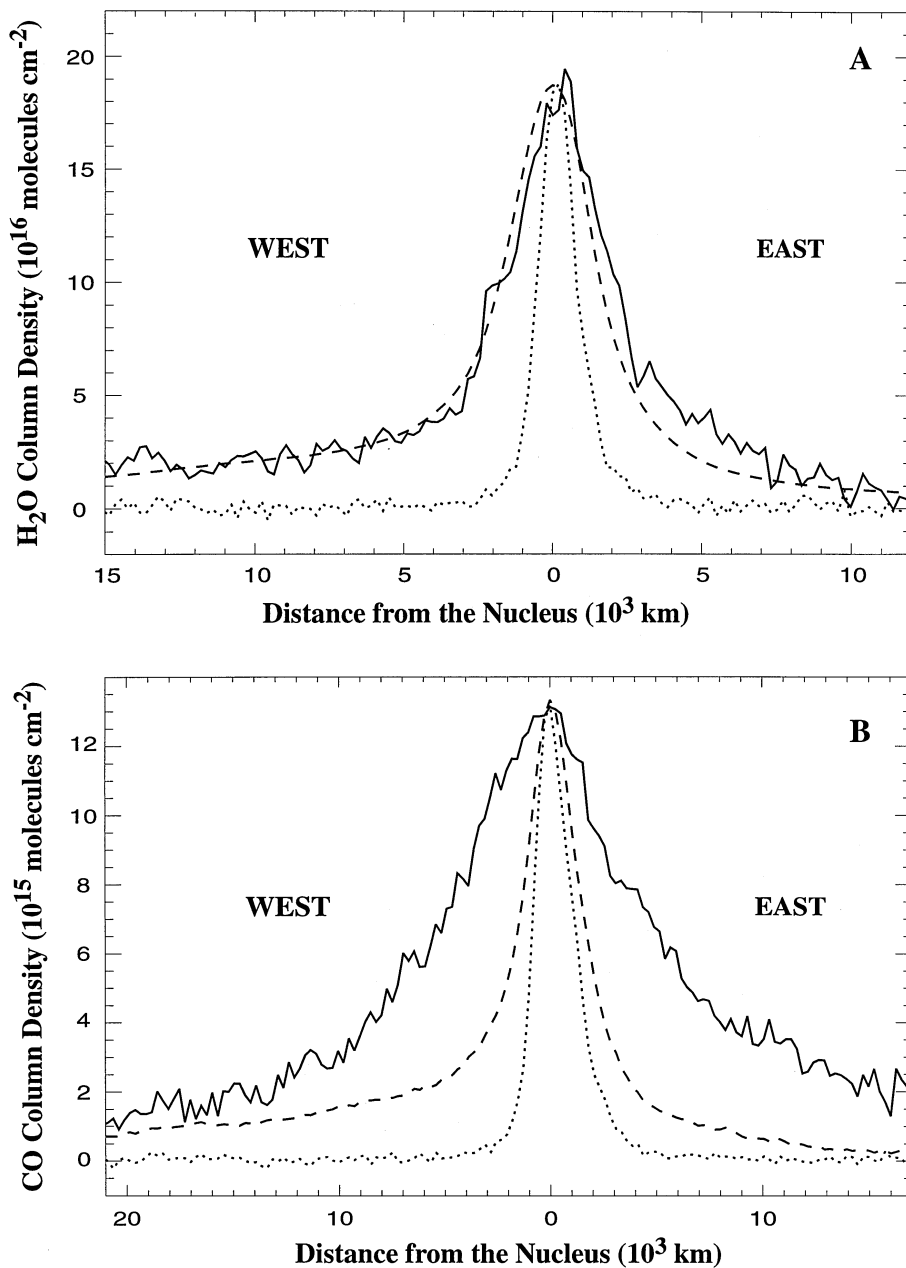
FIG. 2. Spatial profiles for H_2O, CO, and dust. (A) The H_2O column density (solid line), the continuum profile (dashed line), and a stellar profile (PSF; dotted line) on UT Apr. 6.2, 1997. The continuum and stellar profiles were scaled to the peak of the water profile. The water line represented in this figure is the $1_{01}-2_{12}$ line of the $\nu_1 - \nu_2$ band. (B) The CO column density (solid line), scaled continuum profile (dashed line), and scaled stellar profile (dotted line) measured on UT May 1.0, 1997 (DiSanti *et al.* 1999). Note the much broader extent of the CO profile compared with those of H_2O and dust.

relative emission intensities for the observed water lines and take it to equal the temperature distribution of rotational levels in the ground vibrational state (000). We then calculate line g factors using that temperature. We also assume that upper vibrational states can be populated only by pumping from the ground vibrational state, or by cascade from a higher vibrational state (see Appendix). Pump rates from all excited vibrational states are assumed to be negligible. Calculating a rotational temper-

ature is often difficult, since most strong lines have g factors which vary similarly with temperature (Table I), while other lines better suited for a rotational temperature analysis are often too weak or are accidentally coincident with telluric absorption features.

We were nonetheless able to determine rotational temperatures on six dates (Table III). Values were derived on UT Jan. 21.8 and Mar. 1.9 by comparing the intensity ratio for two $\nu_3-\nu_2$

TABLE III
Rotational Temperatures and Production Rates for Water in Comet Hale–Bopp

Date (UT 1997)	R_h (AU)	Δ (AU)	T_{ROT} (K)	Q_{H_2O} (10^{30} molecules s^{-1})
Jan 21.8	1.48	2.18	76^{+16}_{-10}	4.00 ± 0.39
Feb 24.0	1.11	1.57	80^a	8.89 ± 0.89
Mar 1.9	1.06	1.47	85 ± 5	7.63 ± 0.23
Apr 6.2	0.918	1.40	100^a	10.69 ± 1.07
Apr 8.1	0.922	1.42	100^a	9.34 ± 0.93
Apr 9.0	0.925	1.43	100^a	9.33 ± 0.54
Apr 10.2	0.928	1.44	99^{+8}_{-6}	9.99 ± 0.38
Apr 16.0	0.952	1.53	92^{+13}_{-10}	9.12 ± 0.36
Apr 30.0	1.05	1.75	77^{+11}_{-8}	6.76 ± 0.33
May 1.2	1.06	1.77	80^{+13}_{-9}	7.43 ± 0.41
Aug 8.0	2.24	2.90	50^a	$<1.5^b$

[a] Adopted rotational temperatures.
[b] 3σ upper limit.

lines ($F_{0_{00}-1_{01}}/F_{1_{11}-1_{10}}$) to the temperature-dependent ratio of g factors for these lines (since $F_{line} \propto g_{line}$). For dates when the cometary emissions were red-shifted (April and May), the $1_{01}-2_{12}$ and $2_{21}-1_{10}$ lines of the $\nu_1-\nu_2$ band were used (Fig. 3). On other dates, a reasonable rotational temperature was adopted, based on our derived values for H_2O at similar heliocentric distances (Table III). The sensitivity of production rates to adopted rotational temperatures is modest: A difference of 20 K in rotational temperature changes the production rate derived from an individual line by $\sim$5–30% depending on the temperature and the line measured (Table I).
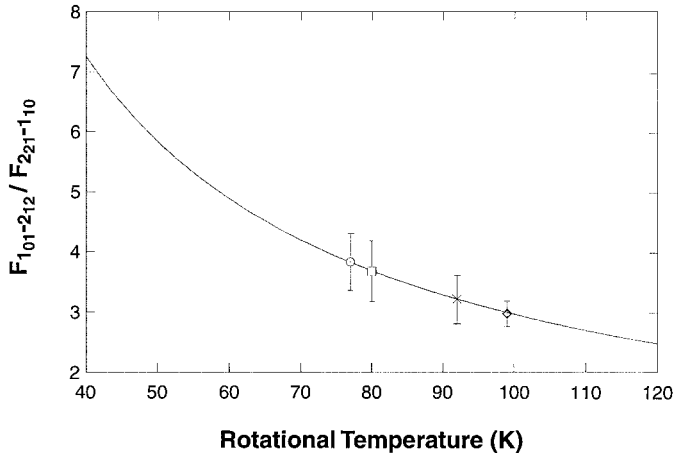
FIG. 3. The rotational temperature of water in Comet Hale–Bopp measured on four dates postperihelion: April 10.2 ($R_h = 0.928$ AU; diamond), April 16.0 ($R_h = 0.952$ AU; cross), April 30.0 ($R_h = 1.05$ AU; circle), and May 1.2 ($R_h = 1.06$ AU; square). Values were derived by comparing the ratio of fluxes between 2 and 12 arcsec from the nucleus for the $1_{01}-2_{12}$ and $2_{21}-1_{10}$ lines of the $\nu_1 - \nu_2$ band (see Table II) to the ratio of their temperature-dependent g factors (see Table I). The expected flux ratio as a function of rotational temperature is given by the solid curve.

6. PRODUCTION RATE GROWTH CURVES

Spatial data may also be examined by generating production rate growth curves (Q curves). These Q curves are generated by stepping a 1×1-arcsec box at 1-arcsec intervals along the spatial direction (along the slit) and calculating a "spherical" production rate from the line flux observed at each step (Figs. 4A and 4B; Dello Russo *et al.* 1998, Magee-Sauer *et al.* 1999). The
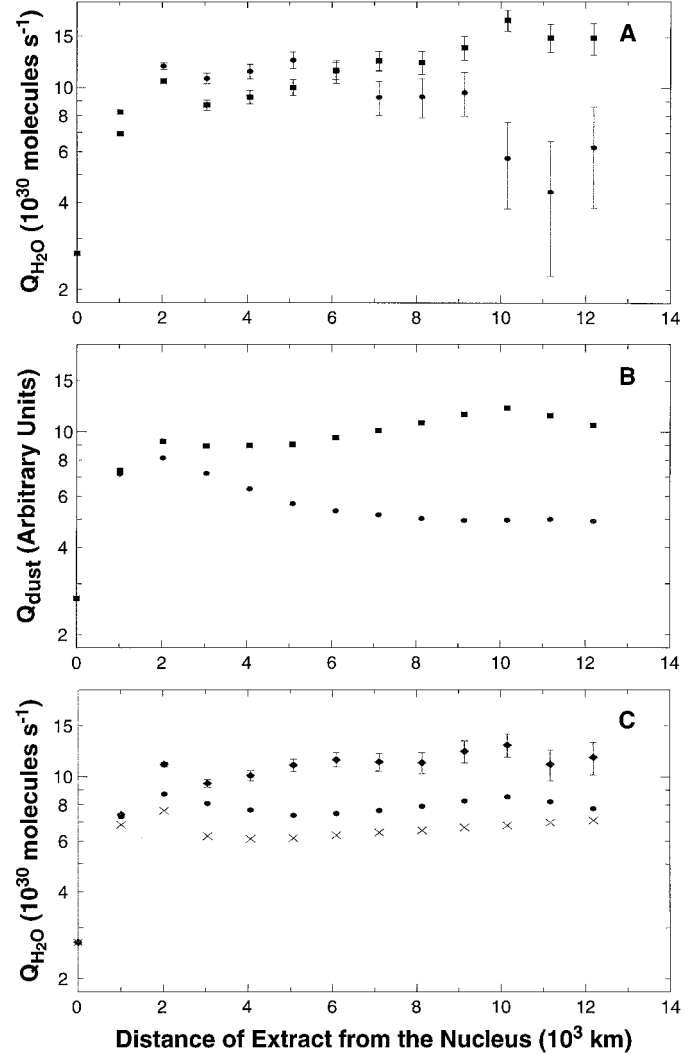
FIG. 4. Production rate growth curves (Q curves) for water and dust in Comet Hale–Bopp on UT Apr. 6.2, 1997. (A) Water Q curve: H_2O spherical production rates derived by stepping 1×1-arcsec extracts east (circles) and west (squares) of the nucleus out to a distance of $\sim$1.2 × 10^4 km (12 arcsec). (B) Continuum Q curve: Dust spherical production rates east (circles) and west (squares) of the nucleus (errors in the spherical production rates for the dust are smaller than the size of the plotted points). (C) Symmetric Q curves for H_2O (diamonds) and dust (circles), derived from a weighted average of east and west extracts (the nucleus-centered dust "production rate" is scaled to the nucleus-centered production rate of water). A scaled Q curve for a stellar profile convolved with a ρ^{-1} distribution (crosses) is also shown to illustrate the effect of nonideal observing conditions, which is primarily responsible for the shape of water and dust Q curves and for lower derived Q values near the nucleus.

production rate (molecules s^{-1}) is given as follows:

$$Q = \frac{4\pi \Delta^2 F_i}{g_i \tau (hc\nu) f(x)}. \tag{1}$$

The photodissociation lifetime τ (s) and line fluorescence efficiency g_i (g factor, photons s^{-1} molecule^{-1}) are both calculated for $R_h = 1$ AU, Δ is the geocentric distance in meters, $hc\nu$ is the energy (J) of a photon with wavenumber ν (cm^{-1}), $f(x)$ is the fraction of molecules expected in the sampled region (x being the fraction of a photodissociation scale length subtended by the beam radius; see appendix of Hoban *et al.* 1991), and F_i is the flux (W m^{-2}) from line i incident atop the terrestrial atmosphere. Transmittance-corrected fluxes for each measured line are given in Table II.

Spherical production rates for water (Fig. 4A) were determined using a reasonable gas outflow velocity ($v_{gas} = 1.1\ R_h^{-0.5}$ km s^{-1}; cf. Biver *et al.* 1997b), and the standard photodissociation lifetime for quiet Sun conditions ($\tau_{H_2O} = 7.7 \times 10^4$ s; Crovisier 1989). We adopt a model in which all H$_2$O is produced at the nucleus and flows outward with spherical symmetry and with uniform velocity. Dust Q curves were generated using the simultaneously obtained continuum profile and assuming $\tau_{dust} \gg \tau_{H_2O}$ (Fig. 4B). Symmetric production rates for each water line (diamonds, Fig. 4C) were determined by taking a weighted mean of corresponding spherical production rates east and west of the nucleus (Q_{dust} is scaled to Q_{H_2O} on the nucleus in Fig. 4C).

Dust and water Q curves show derived production rates which are lower for the nucleus-centered extract than for extracts offset from the nucleus. This is not surprising since, as discussed in section 4, nonideal observing conditions cause departures from a ρ^{-1} spatial distribution near the nucleus. Can these effects completely explain the shapes of the Q curves? The effect of a real PSF on derived production rates was investigated by generating a Q curve for a stellar profile convolved with a ρ^{-1} distribution (crosses in Fig. 4C) and comparing it to Q curves for water and dust. Although conditions were variable and probably not identical for stellar and cometary observations (which were taken typically 1–8 h apart), the similar behavior of the water, dust, and PSF Q curves shows that nonideal observing conditions are primarily responsible for the shapes of the water and dust Q curves and for lower production rates derived from nucleus-centered extracts. Because the PSF can change between cometary and stellar observations, it is difficult to quantify the contribution of nonideal observing conditions to the shape of a Q curve, however, it is clear that production rates determined within the FWHM of a representative PSF are unreliable.

For this reason, the "global" production rate determined from each individual line of water was taken from a weighted average of symmetric production rates over the range 2–12 arcsec from the nucleus (Fig. 4C). Although asymmetries will likely have a small effect on our derived production rates, this method has been shown to be a valid approach to first order (cf. Xie and Mumma 1996). Global production rates for a particular date

(Table III) are represented by the weighted average of production rates for all strong lines measured on that date.

Although east/west averaged Q curves for water, dust, and the PSF reach their terminal values at about the same distance from the nucleus on UT April 6.2, the water curve terminates at a slightly higher value relative to the nucleus-centered point than does the dust or PSF curve (Fig. 4C). The observed behavior is formally consistent with most water in the coma being released directly from the nucleus, with partial release of water from a distributed source (e.g., icy grains) possible within 1000–2000 km of the nucleus.

A small distributed source for water is not the only possible explanation for the different behavior of the water, dust, and PSF Q curves. As mentioned earlier, the difference in the PSF Q curve may be due to observing conditions which were not equivalent for the star and comet. The differences between water and dust Q curves could be caused by more efficient isotropization of water close to the nucleus (cf. Figs. 4A and 4B) or by differential acceleration of dust and water. Opacity effects could also cause the water Q curve to terminate at a slightly higher value than the dust or PSF curve. The distance from the nucleus (along a line of sight centered on the nucleus) where the H$_2$O coma becomes optically thick was estimated by assuming that opacity effects in the pumps dominate opacity effects in the cascade (see Dello Russo *et al.* 1998 for formalism). Opacity is estimated to be negligible beyond ∼200 km (0.2 arcsec) from the nucleus for line in the 111–100 and 100–010 hot bands (due to opacity in the 000–111 and 000–100 pumps) and negligible beyond ∼1000 km for lines in the 001–010 hot band (due to opacity in the 000–001 pump). Although not severe, opacity effects could suppress the derived water production rate for a nucleus-centered extract relative to the corresponding value for the dust or PSF. Since optical depth has a greater influence on derived gas production rates near the nucleus than on dust production rates, a water Q curve may increase by a slightly greater factor than the associated dust (or PSF) Q curve, even in the absence of any distributed source contribution. For these reasons, we do not claim to have detected a distributed source for water in Comet Hale–Bopp. Quantifying effects due to opacity and outflow asymmetry require detailed modeling and are beyond the scope of this paper.

7. HELIOCENTRIC DEPENDENCE OF GLOBAL PRODUCTION RATES

A global production rate for water on each individual date (Table III) was generally derived from multiple ro-vibrational lines and often using lines from different hot bands (Table II). The self-consistency of our data processing algorithms and fluorescence efficiency models for H$_2$O is demonstrated by the agreement among production rates derived for different lines in a given hot band on the same date and for lines from the three different hot bands (Table II). Errors were evaluated line-by-line for each date. The (1σ) errors in line flux reported in Table II are
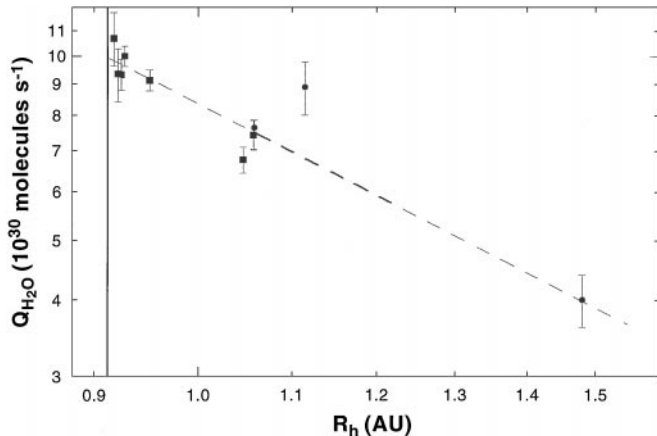
FIG. 5. Evolution of the water production rate in Comet Hale–Bopp with heliocentric distance R_h. The solid vertical line represents the heliocentric distance at perihelion. The dashed line is the heliocentric dependence $Q_{H_2O} = (8.35 \pm 0.13) \times 10^{30} \, [R_h^{(-1.88 \pm 0.18)}]$ molecules s^{-1}, derived from a least squares fit to our measured values preperihelion (circles) and postperihelion (squares). Based on our fit, we estimate the absolute 1σ uncertainty in Q_{H_2O} to be $\pm 0.41 \times 10^{30}$ and $\pm 0.91 \times 10^{30}$ molecules s^{-1} at 1.0 and 1.5 AU, respectively.

derived from the deviation of the water spatial profile (Fig. 2A) from a fitted curve (gaussian + polynomial). The 1σ uncertainty in global production rate for each line in Table II represents the standard deviation of the mean production rate over the range 2–12 arcsec from the nucleus (e.g., Fig. 4C). This includes factors such as spatial variations in rotational temperature and outflow velocity, and other factors which cause deviations from our idealized gas outflow model. On dates where rotational temperatures were not determined from our data, a minimum uncertainty of 10% in production rate was assumed for each measured line.

Our water production rates are shown vs heliocentric distance in Fig. 5. A least squares fit to values on our 10 dates yielded $Q_{H_2O} = (8.35 \pm 0.13) \times 10^{30} \, [R_h^{(-1.88 \pm 0.18)}]$ molecules s^{-1}. This is formally consistent with an insolation-limited dependence of R_h^{-2}. Separate pre- and postperihelion dependences were not obtained due to insufficient sampling preperihelion and insufficient heliocenric coverage postperihelion. Similar heliocentric dependences were derived for native CO production ($R_h^{(-1.73 \pm 0.26)}$ between 4.1 and 0.9 AU, DiSanti *et al.* 1999), and for dust at millimeter wavelengths ($R_h^{(-1.7 \pm 0.2)}$ between 2.5 and 0.9 AU, Jewitt and Matthews 1999). This implies that the mass loss ratio for native CO, water, and dust remained constant within 1.5 AU of the Sun, as expected if water release controls the production of these species. Considering these three species alone, the mass ratio of dust to ice released from the nucleus near perihelion was 5.1 ± 1.2. This is consistent with the value (≥ 5) derived by Jewitt and Matthews (1999).

Production rates for OH at radio wavelengths near perihelion agree with our measurements. However our derived values on Jan. 21.8, Feb. 24.0, and Mar. 1.9 are about a factor of two larger than the radio OH results in this time frame (Colom *et al.* 1997),

and about a factor of three larger than the derived Q_{OH} from ultraviolet measurements between 1.55 and 1.20 AU preperihelion (Schleicher *et al.* 1997). The reasons for this disagreement are unclear, but could be related to variable cometary activity, the models applied to the OH observations, or to unrecognized effects in our own models. As a result, our derived heliocentric dependence for water production rates at $R_h < 1.5$ AU is less steep than that obtained for OH at radio wavelengths ($\sim R_h^{-3.7}$ at $R_h \leq 1.3$ AU; Colom *et al.* 1997). The fact that our heliocentric dependence for H_2O agrees with that for native CO and millimeter-sized dust, lends support to the soundness of our results.

Water was not detected on UT Aug. 8.0, 1997 ($R_h = 2.24$ AU postperihelion), but a 3σ upper limit to the production rate was obtained that is slightly below our derived heliocentric dependence. This upper limit was derived from the observed line flux in a 1×1-arcsec extract centered on the nucleus. We assume this to be a factor of three lower than the true line flux, based on the increase seen for our ethane Q curve on Aug. 8.0 (Dello Russo *et al.* in preparation). This upper limit is consistent with an inferred water production rate of $(2.6 \pm 0.4) \times 10^{29}$ molecules s^{-1} from SWUIS UV/VIS imager measurements of OH aboard the Shuttle Discovery between Aug. 9 and 15 (Stern *et al.* 1999), and with a predicted decrease in the water sublimation rate beyond ~ 2 AU if one considers the comet as a very large isothermal particle (Jewitt *et al.* 1996). However, the lack of postperihelion coverage between $R_h = 1.06$ and $R_h = 2.24$ AU makes a definitive interpretation difficult.

8. SUMMARY

Historically, direct detection of water from groundbased observatories has not been possible due to severe atmospheric extinction. To avoid this problem, we developed a general method for observing water from the ground by targeting lines in nonresonance fluorescence. This method is most advantageous for relatively bright comets near perihelion since multiple water lines in different hot bands can be detected and spatially mapped in the inner coma with high signal-to-noise ratios. This reduces the dependence on model assumptions compared with techniques which infer water production from daughter products. At larger heliocentric and geocentric distances indirect methods enjoy an advantage in sensitivity since detection of relatively weak hotband lines becomes difficult.

The high spatial resolution afforded by CSHELL provided the opportunity to compare the distributions of volatiles and dust in the coma of Comet Hale–Bopp. Comparing simultaneously obtained profiles of volatiles and dust can provide a qualitative means of determining the presence or absence of a significant distributed source contribution. The spatial profile for volatiles (and dust) released directly from the nucleus should fall off approximately as ρ^{-1} (outside the region affected by nonideal observing conditions), while the presence of a distributed source will result in a broader distribution. Our spatial

profiles for H_2O and dust are consistent with the release of both directly from the nucleus of Hale–Bopp within 1.5 AU of the Sun.

Spatial data may also be presented by generating Q curves. Derived production rates from nucleus-centered extracts are always lower than those derived from extracts centered off the nucleus due to nonideal observing conditions. The extent of the affected region is represented by the FWHM of a stellar PSF (assuming the observing conditions for the star and comet were similar). For this reason, we determine global production rates outside this affected region (in this case between 2 and 12 arcsec from the nucleus). Comparison of Q curves for water, dust, and a real PSF show that most (perhaps all) water is released directly from the nucleus within 1.5 AU of the Sun. A small contribution from distributed sources (icy grains, ion–molecule chemistry, etc.) is formally possible within $\sim$1000–2000 km of the nucleus. However, differentiating competing effects which cause deviations from ρ^{-1} within this region is problematic, so we do not claim to have detected a distributed source for water in Comet Hale–Bopp. This differs from the behavior at large heliocentric distances, where more volatile species (e.g., CO) controlled the activity of Hale–Bopp and most water was probably released from a distributed source of icy grains (Jewitt *et al.* 1996, Biver *et al.* 1996, Davies *et al.* 1997).

We derive a heliocentric dependence $Q_{H_2O} = (8.35 \pm 0.13) \times 10^{30} [R_h^{(-1.88 \pm 0.18)}]$ molecules s^{-1} for Hale–Bopp (Fig. 5). When compared with release of native CO and dust (DiSanti *et al.* 1999, Jewitt and Matthews 1999), our results imply a dust to ice mass ratio in the nucleus of 5.1 ± 1.2. The measured heliocentric dependences for production of CO and millimeter sized dust agree with our measurement for water, implying that water controls the release of these species within 1.5 AU of the Sun.

Our water abundances provide a benchmark with which water production rates inferred by indirect methods can be compared. They provide a standard for other volatile species in Hale–Bopp which, when compared to interstellar and nebular material, will help constrain the origin of cometary ices and their processing histories.

APPENDIX: DETERMINATION OF G-FACTORS FOR H_2O HOT-BAND EMISSIONS

In nonresonance fluorescence, direct absorption of solar photons excites molecules from the ground vibrational state (000) to a higher vibrational state, followed by cascade into an intermediate state. For example, the 111–100 ($\nu_1 + \nu_2 + \nu_3 - \nu_1$) hot band is the result of a pump from 000 to 111 (the total pump rate $P(000-111) = 1.97 \times 10^{-6}$ s^{-1}) followed by cascade into 100 with 12.1% efficiency. The 100 state is not significantly populated at 300 K, so laboratory absorption strengths are not available for the 111–100 transition. We therefore take the radiative transition probabilities for 111–100 from those for 011–000 (i.e., we assume that the vibrational wavefunctions are separable). An analogous approach is used for other transitions from 111 that terminate on highly excited states. Two other hot bands (001–010 and 100–010) are also seen in our data.

The upper vibrational level (001) of the 001–010 ($\nu_3 - \nu_2$) hot band is populated primarily ($\sim$97%) by a direct pump from 000 (the total pump rate $P(000-001) = 2.81 \times 10^{-4}$ s^{-1}; Bockelée-Morvan and Crovisier 1989). A small con-

tribution ($\sim$3%) to the population of the 001 level is provided by cascade from the 101 and 011 states. Cascade from 001 to 010 proceeds with 2.65% efficiency (Bockelée-Morvan and Crovisier 1989).

The upper vibrational level (100) of the 100–010 ($\nu_1 - \nu_2$) hot band is populated by two major pathways: (1) A direct pump from 000 and (2) a pump from 000 to 101 followed by cascade into 100 with 23.0% efficiency (Bockelée-Morvan and Crovisier 1989). Pump rates for 000–100 and 000–101 are calculated from laboratory absorption strengths. Transition probabilites for 101–100 are taken from measured band strengths for 001–000, and vibrational branching ratios for 100–010 are based on measured absorption strengths for 100–010 and 100–000. Laboratory absorption strengths are used to calculate radiative transition probabilities for 100–010, while the transition probabilities for 101–100 are taken from the measured band strengths for 001–000. We use the following values for vibrational band pump rates and vibrational branching ratios (BR) taken from Bockelée-Morvan and Crovisier (1989):

$$P(000-100) = 1.01 \times 10^{-5} \text{ s}^{-1}$$
$$P(000-101) = 3.04 \times 10^{-5} \text{ s}^{-1}.$$

Vibrational branching ratios:

$$BR(101-100) = 0.720$$
$$BR(100-010) = 0.230.$$

Fluorescence efficiencies (g factors, s^{-1}) are calculated as follows. We first establish populations for all rotational levels in the 000 vibrational state by assuming a Boltzmann distribution at a specified rotational temperature (the populations of all excited vibrational states are initially assumed to be zero). Rotational branching ratios are then calculated using Einstein coefficients for each ro-vibrational transition, taken from the HITRAN-1992 Molecular Data Base (Rothman *et al.* 1992). Next, three steps are considered, leading to the g factor for a ro-vibrational line: (A) direct pump from 000 to 100, (B) pumping from 000 to 101 with subsequent cascade into 100, (C) cascade from 100 into 010. An example is given below for the $2_{12}-3_{03}$ line at 2003.00 cm^{-1}.

A. Direct Pump from 000 (Ground Vibrational State) to the 2_{12} Level of 100

The 2_{12} level of 100 can be pumped from four rotational levels in 000 (i.e., $1_{01}, 2_{21}, 3_{03}$, and 3_{21}), whose populations vary with temperature. The individual pumping rates P (s^{-1}) and their sum $[P(000-100)_{2_{12}}]$ are given below for temperatures (K) of interest.

Temp. (K)	$P(1_{01}-2_{12})$	$P(2_{21}-2_{12})$	$P(3_{03}-2_{12})$	$P(3_{21}-2_{12})$	$P(000-100)_{2_{12}}$
40	1.74×10^{-6}	2.98×10^{-8}	6.75×10^{-8}	3.62×10^{-9}	1.84×10^{-6}
50	1.48×10^{-6}	5.64×10^{-8}	1.29×10^{-7}	1.19×10^{-8}	1.68×10^{-6}
60	1.26×10^{-6}	8.18×10^{-8}	1.89×10^{-7}	2.50×10^{-8}	1.56×10^{-6}
70	1.08×10^{-6}	1.03×10^{-7}	2.40×10^{-7}	4.11×10^{-8}	1.46×10^{-6}
80	9.31×10^{-7}	1.18×10^{-7}	2.76×10^{-7}	5.74×10^{-8}	1.38×10^{-6}
90	8.08×10^{-7}	1.28×10^{-7}	3.01×10^{-7}	7.26×10^{-8}	1.31×10^{-6}
100	7.08×10^{-7}	1.34×10^{-7}	3.15×10^{-7}	8.59×10^{-8}	1.24×10^{-6}
120	5.49×10^{-7}	1.36×10^{-7}	3.21×10^{-7}	1.05×10^{-7}	1.11×10^{-6}
150	3.95×10^{-7}	1.27×10^{-7}	3.03×10^{-7}	1.19×10^{-7}	9.44×10^{-7}
296	1.24×10^{-7}	6.76×10^{-8}	1.62×10^{-7}	9.07×10^{-8}	4.44×10^{-7}

B. Pump into 101 followed by Cascade into 100

1. Pump into the 101 vibrational state. Four rotational levels ($1_{11}, 2_{11}, 3_{13}$, and 3_{31}) in the 101 vibrational state can populate the 2_{12} level of the 100 vibrational state upon cascade. All pumps from rotational levels in 000 to these levels in 101 are needed. Rates (s^{-1}) for populating each of these rotational levels in 101 are given below.

	Direct pumping rates (s^{-1}) into the 1_{11} rotational level of 101		
Temp. (K)	$P(1_{10}-1_{11})$	$P(2_{12}-1_{11})$	$P(000-101)_{1_{11}}$
40	2.51×10^{-6}	6.87×10^{-7}	3.20×10^{-6}
50	2.44×10^{-6}	8.75×10^{-7}	3.32×10^{-6}
60	2.29×10^{-6}	9.79×10^{-7}	3.27×10^{-6}
70	2.10×10^{-6}	1.02×10^{-6}	3.12×10^{-6}
80	1.92×10^{-6}	1.02×10^{-6}	2.94×10^{-6}
90	1.75×10^{-6}	1.01×10^{-6}	2.76×10^{-6}
100	1.60×10^{-6}	9.77×10^{-7}	2.58×10^{-6}
120	1.34×10^{-6}	8.94×10^{-7}	2.23×10^{-6}
150	1.06×10^{-6}	7.74×10^{-7}	1.83×10^{-6}
296	4.72×10^{-7}	4.10×10^{-7}	8.82×10^{-7}

	Direct pumping rates (s^{-1}) into the 2_{11} rotational level of 101				
	$P(1_{10}-2_{11})$	$P(2_{12}-2_{11})$	$P(3_{12}-2_{11})$	$P(3_{30}-2_{11})$	$P(000-101)_{2_{11}}$
40	3.80×10^{-6}	3.35×10^{-7}	4.52×10^{-8}	1.59×10^{-12}	4.18×10^{-6}
50	3.71×10^{-6}	4.28×10^{-7}	1.13×10^{-7}	8.91×10^{-12}	4.25×10^{-6}
60	3.47×10^{-6}	4.78×10^{-7}	1.99×10^{-7}	2.68×10^{-11}	4.15×10^{-6}
70	3.19×10^{-6}	4.99×10^{-7}	2.86×10^{-7}	5.65×10^{-11}	3.98×10^{-6}
80	2.91×10^{-6}	5.00×10^{-7}	3.65×10^{-7}	9.62×10^{-11}	3.78×10^{-6}
90	2.65×10^{-6}	4.92×10^{-7}	4.33×10^{-7}	1.43×10^{-10}	3.58×10^{-6}
100	2.43×10^{-6}	4.77×10^{-7}	4.88×10^{-7}	1.92×10^{-10}	3.40×10^{-6}
120	2.03×10^{-6}	4.37×10^{-7}	5.59×10^{-7}	2.89×10^{-10}	3.03×10^{-6}
150	1.61×10^{-6}	3.78×10^{-7}	6.06×10^{-7}	4.09×10^{-10}	2.59×10^{-6}
296	7.15×10^{-7}	2.00×10^{-7}	5.01×10^{-7}	5.75×10^{-10}	1.42×10^{-6}

	Direct pumping rates (s^{-1}) into the 3_{13} rotational level of 101					
	$P(2_{12}-3_{13})$	$P(3_{12}-3_{13})$	$P(3_{30}-3_{13})$	$P(4_{14}-3_{13})$	$P(4_{32}-3_{13})$	$P(000-101)_{3_{13}}$
40	1.84×10^{-6}	1.34×10^{-8}	8.41×10^{-12}	1.51×10^{-8}	7.45×10^{-13}	1.87×10^{-6}
50	2.35×10^{-6}	3.36×10^{-8}	4.72×10^{-11}	5.46×10^{-8}	8.41×10^{-12}	2.44×10^{-6}
60	2.62×10^{-6}	5.90×10^{-8}	1.42×10^{-10}	1.23×10^{-7}	4.02×10^{-11}	2.80×10^{-6}
70	2.74×10^{-6}	8.49×10^{-8}	2.99×10^{-10}	2.10×10^{-7}	1.18×10^{-10}	3.04×10^{-6}
80	2.75×10^{-6}	1.08×10^{-7}	5.09×10^{-10}	3.07×10^{-7}	2.59×10^{-10}	3.17×10^{-6}
90	2.70×10^{-6}	1.29×10^{-7}	7.56×10^{-10}	4.03×10^{-7}	4.66×10^{-10}	3.23×10^{-6}
100	2.62×10^{-6}	1.45×10^{-7}	1.02×10^{-9}	4.93×10^{-7}	7.34×10^{-10}	3.26×10^{-6}
120	2.40×10^{-6}	1.66×10^{-7}	1.53×10^{-9}	6.40×10^{-7}	1.39×10^{-9}	3.21×10^{-6}
150	2.07×10^{-6}	1.80×10^{-7}	2.17×10^{-9}	7.85×10^{-7}	2.49×10^{-9}	3.04×10^{-6}
296	1.10×10^{-6}	1.49×10^{-7}	3.04×10^{-9}	8.28×10^{-7}	5.53×10^{-9}	2.09×10^{-6}

	Direct pumping rates (s^{-1}) into the 3_{31} rotational level of 101					
	$P(2_{12}-3_{31})$	$P(3_{12}-3_{31})$	$P(3_{30}-3_{31})$	$P(4_{14}-3_{31})$	$P(4_{32}-3_{31})$	$P(000-101)_{3_{31}}$
40	5.06×10^{-9}	2.27×10^{-10}	2.13×10^{-9}	5.10×10^{-12}	2.45×10^{-11}	7.45×10^{-9}
50	6.45×10^{-9}	5.69×10^{-10}	1.20×10^{-8}	1.85×10^{-11}	2.77×10^{-10}	1.93×10^{-8}
60	7.21×10^{-9}	9.98×10^{-10}	3.59×10^{-8}	4.16×10^{-11}	1.32×10^{-9}	4.55×10^{-8}
70	7.52×10^{-9}	1.43×10^{-9}	7.58×10^{-8}	7.13×10^{-11}	3.90×10^{-9}	8.87×10^{-8}
80	7.54×10^{-9}	1.83×10^{-9}	1.29×10^{-7}	1.04×10^{-10}	8.52×10^{-9}	1.47×10^{-7}
90	7.41×10^{-9}	2.17×10^{-9}	1.92×10^{-7}	1.37×10^{-10}	1.53×10^{-8}	2.17×10^{-7}
100	7.19×10^{-9}	2.45×10^{-9}	2.58×10^{-7}	1.67×10^{-10}	2.42×10^{-8}	2.92×10^{-7}
120	6.58×10^{-9}	2.81×10^{-9}	3.87×10^{-7}	2.17×10^{-10}	4.58×10^{-8}	4.42×10^{-7}
150	5.70×10^{-9}	3.05×10^{-9}	5.49×10^{-7}	2.66×10^{-10}	8.19×10^{-8}	6.40×10^{-7}
296	3.02×10^{-9}	2.52×10^{-9}	7.71×10^{-7}	2.81×10^{-10}	1.82×10^{-7}	9.59×10^{-7}

2. Cascade from 101 to 100. The vibrational branching ratio for cascade from 101 to 100 is 0.720. Rotational branching ratios are determined by accounting for all possible transitions from the relevant upper rotational states (1_{11}, 2_{11}, 3_{13}, and 3_{31}) to lower rotational states. There are 16 total transitions. The four which populate the 2_{12} level in 100 are in **bold** type (with corresponding rotational branching ratios, e.g., BR(101_{111}–100_{212}) = 0.504). Note that for cascade, the upper rotational level is listed first.

Rotational levels (101–100 band)	Rotational BR
1_{11}–1_{10}	0.496
1_{11}–2_{12}	**0.504**
2_{11}–1_{10}	0.279
2_{11}–2_{12}	**0.160**
2_{11}–3_{12}	0.556
2_{11}–3_{30}	0.005
3_{13}–2_{12}	**0.353**
3_{13}–3_{12}	0.092
3_{13}–3_{30}	0.001
3_{13}–4_{14}	0.549
3_{13}–4_{32}	0.004
3_{31}–2_{12}	**0.002**
3_{31}–3_{12}	0.002
3_{31}–3_{30}	0.732
3_{31}–4_{14}	0.000
3_{31}–4_{32}	0.264

C. Cascade from 100 to 010

Combining the above information, *g* factors for 100–010 hot-band emission can be calculated as a function of temperature:

$$g_T(2_{12}-3_{03}) = [P(000-100)_{212} + \{P(000-101)_{111}(BR(101_{111}-100_{212}))$$
$$+ P(000-101)_{211}(BR(101_{211}-100_{212})) + P(000-101)_{313}$$
$$\times (BR(101_{313}-100_{212})) + P(000-101)_{331}$$
$$\times (BR(101_{331}-100_{212}))\}(BR(101-100))]$$
$$\times (BR(100-010))(BR(100_{212}-010_{303})).$$

The vibrational branching ratio for cascade from 100 to 010 is 0.230, based on measured laboratory absorption strengths. The rotational branching ratio for 2_{12}–3_{03} is 0.2865. For the 2_{12}–3_{03} line at $T = 40$ K this becomes

$$g_{40K}(2_{12}-3_{03}) = [1.84 \times 10^{-6} + \{3.20 \times 10^{-6}(0.504)$$
$$+ 4.18 \times 10^{-6}(0.160) + 1.87 \times 10^{-6}(0.353)$$
$$+ 7.45 \times 10^{-9}(0.002)\}(0.720)](0.230)(0.2865)$$
$$= 2.61 \times 10^{-7}.$$

Temp. (K)	$g(2_{12}-3_{03})$ (s^{-1})
40	2.61×10^{-7}
50	2.63×10^{-7}
60	2.59×10^{-7}
70	2.52×10^{-7}
80	2.43×10^{-7}
90	2.33×10^{-7}
100	2.24×10^{-7}
120	2.03×10^{-7}
150	1.76×10^{-7}
296	9.61×10^{-8}

REFERENCES

Biver, N., D. Bockelée-Morvan, P. Colom, J. Crovisier, J. K. Davies, W. R. F. Dent, D. Despois, E. Gérard, E. Lellouch, H. Rauer, R. Moreno, and G. Paubert 1997a. Evolution of the outgassing of Comet Hale–Bopp (C/1995 O1) from radio observations. *Science* **275**, 1915–1918.

Biver, N., D. Bockelée-Morvan, P. Colom, J. Crovisier, B. Germain, E. Lellouch, J. K. Davies, W. R. F. Dent, R. Moreno, G. Paubert, J. Wink, D. Despois, D. C. Lis, D. Mehringer, D. Benford, M. Gardner, T. G. Phillips, M. Gunnarsson, H. Rickman, A. Winnberg, P. Bergman, L. E. B. Johansson, and H. Rauer 1997b. Long term evolution of the outgassing of Comet Hale–Bopp from radio observations. *Earth, Moon, Planets* **78**, 5–11.

Biver, N., H. Rauer, D. Despois, R. Moreno, G. Paubert, D. Bockelée-Morvan, P. Colom, J. Crovisier, E. Gérard, and L. Jorda 1996. Substantial outgassing of CO from Comet Hale–Bopp at large heliocentric distance. *Nature* **380**, 137–139.

Bockelée-Morvan, D., and J. Crovisier 1989. The nature of the 2.8-μm emission feature in cometary spectra. *Astron. Astrophys.* **216**, 278–283.

Colom, P., E. Gérard, J. Crovisier, D. Bockelée-Morvan, N. Biver, and H. Rauer 1997. Observations of the OH radical in Comet C/1995 O1 (Hale–Bopp) with the Nancay radio telescope. *Earth, Moon, Planets* **78**, 37–43.

Combes, M., V. I. Moroz, J. Crovisier, T. Encrenaz, J.-P. Bibring, A. V. Gringoriev, N. F. Sanko, N. Coron, J. F. Crifo, R. Gispert, D. Bockelée-Morvan, Yu. V. Nikolsky, V. A. Krasnopolsky, T. Owen, C. Emerich, J. M. Lamarre, and F. Rocard 1988. The 2.5- to 12-μm spectrum of Comet Halley from the IKS-VEGA experiment. *Icarus* **76**, 404–436.

Combi, M. R., M. E. Brown, P. D. Feldman, H. U. Keller, R. R. Meier, and W. H. Smyth 1998. Hubble Space Telescope ultraviolet imaging and high-resolution spectroscopy of water photodissociation products in Comet Hyakutake (C/1996 B2). *Astrophys. J.* **494**, 816–821.

Crovisier, J. 1989. The photodestruction of water in cometary atmospheres. *Astron. Astrophys.* **213**, 459–464.

Crovisier, J., N. Biver, D. Bockelée-Morvan, P. Colom, L. Jorda, E. Lellouch, G. Paubert, and D. Despois 1995. Carbon monoxide outgassing from Comet P/Schwassmann–Wachmann I. *Icarus* **115**, 213–216.

Crovisier, J., K. Leech, D. Bockelée-Morvan, T. Y. Brooke, M. S. Hanner, B. Altieri, H. U. Keller, and E. Lellouch 1997. The spectrum of Comet Hale–Bopp (C/1995 O1) observed with the Infrared Space Observatory at 2.9 astronomical units from the Sun. *Science* **275**, 1904–1907.

Davies, J. K., T. L. Roush, D. P. Cruikshank, M. J. Bartholomew, T. R. Geballe, T. Owen, and C. de Bergh 1997. The detection of water ice in Comet Hale–Bopp. *Icarus* **127**, 238–245.

Dello Russo, N., M. A. DiSanti, M. J. Mumma, K. Magee-Sauer, and T. W. Rettig 1998. Carbonyl sulfide in Comets C/1996 B2 (Hyakutake) and C/1995 O1 (Hale–Bopp): Evidence for an extended source in Hale–Bopp. *Icarus* **135**, 377–388.

DiSanti, M. A., M. J. Mumma, N. Dello Russo, K. Magee-Sauer, R. Novak, and T. W. Rettig 1999. Identification of two sources of carbon monoxide in Comet Hale–Bopp. *Nature* **399**, 662–665.

Eberhardt, P., D. Krankowsky, W. Schulte, U. Dolder, P. Lammerzahl, J. J. Berthelier, J. Woweries, U. Stubbemann, R. R. Hodges, J. H. Hoffman, and J. M. Illiano 1987. The CO and N$_2$ abundance in Comet P/Halley. *Astron. Astrophys.* **187**, 481–484.

Fink, U., and M. D. Hicks 1996. A survey of 39 comets using CCD spectroscopy. *Astrophys. J.* **459**, 729–743.

Greenberg, J. M., and A. Li 1998. From interstellar dust to comets: The extended CO source in Comet Halley. *Astron. Astrophys.* **332**, 374–384.

Greene, T. P., A. T. Tokunaga, D. W. Toomey, and J. B. Carr 1993. CSHELL: A high spectral resolution 1–5 μm cryogenic echelle spectrograph for the IRTF. *Proc. SPIE* **1946**, 313–324.

Hoban, S., M. J. Mumma, D. C. Reuter, M. DiSanti, and R. R. Joyce 1991. A tentative identification of methanol as the progenitor of the 3.52-μm emission feature in several comets. *Icarus* **93**, 122–134.

Jewitt, D., M. Senay, and H. Matthews 1996. Observations of carbon-monoxide in Comet Hale–Bopp. *Science* **271**, 1110–1113.

Jewitt, D., and H. E. Matthews 1999. Particulate mass loss from Comet Hale–Bopp. *Astron. J.* **117**, 1056–1062.

Kunde, V. G., and J. C. Maguire 1974. Direct integration transmittance model. *J. Quant. Spectrosc. Radiat. Transfer* **14**, 803–817.

Magee-Sauer, K., M. J. Mumma, M. A. DiSanti, N. Dello Russo, and T. W. Rettig 1999. Infrared spectroscopy of the ν_3 band of hydrogen cyanide in C/1995 O1 Hale–Bopp. *Icarus* **142**, 498–508.

Mumma, M. J., M. A. DiSanti, A. Tokunaga, and E. E. Roettger 1995. Ground-based detection of water in Comet Shoemaker–Levy 1992 XIX: Probing cometary parent molecules by hot-band fluorescence. *Bull. Am. Astron. Soc.* **27**, 1144.

Mumma, M. J., M. A. DiSanti, N. Dello Russo, M. Fomenkova, K. Magee-Sauer, C. D. Kaminski, and D. X. Xie 1996. Detection of abundant ethane and methane, along with carbon monoxide and water, in Comet C/1996 B2 Hyakutake: Evidence for interstellar origin. *Science* **272**, 1310–1314.

Mumma, M. J., H. A. Weaver, H. P. Larson, D. S. Davis, and M. Williams 1986. Detection of water vapor in Halley's comet. *Science* **232**, 1523–1528.

Rothman, L. S., R. R. Gamache, R. H. Tipping, C. P. Rinsland, M. A. H. Smith, D. Chris Benner, V. Malathy Devi, J.-M. Flaud, C. Camy-Peyret, A. Perrin, A. Goldman, S. T. Massie, L. R. Brown, and R. A. Toth 1992. The HITRAN molecular database: Editions of 1991 and 1992. *J. Quant. Spectrosc. Radiat. Transfer* **48**, 469–507.

Schleicher, D. G., and M. F. A'Hearn 1982. OH fluorescence in comets: Fluorescence efficiency of the ultaviolet bands. *Astrophys. J.* **258**, 864–877.

Schleicher, D. G., S. M. Lederer, R. L. Millis, and T. L. Farnham 1997. Photometric behavior of Comet Hale–Bopp (C/1995 O1) before perihelion. *Science* **275**, 1913–1915.

Senay, M. C., and D. Jewitt 1994. Coma formation driven by CO release from Comet Schwassmann–Wachmann I. *Nature* **371**, 229–231.

Stern, S. A., W. B. Colwell, M. C. Festou, P. M. Tamblyn, J. W. Parker, D. C. Slater, P. R. Weissman, and L. J. Paxton 1999. Comet Hale–Bopp (C/1995 O1) near 2.3 AU postperihelion: Southwest Ultraviolet Imaging System measurements of the H_2O and dust production, *Astron. J.* **118**, 1120–1125.

Tacconi-Garman, L. E., P. F. Schloerb, and M. J. Claussen 1990. High spectral resolution observations and kinematic modeling of the 1667 MHz hyperfine transition of OH in Comets Halley (1982i), Giacobini–Zinner (1984e), Hartley–Good (1985l), Thiele (1985m) and Wilson (1986l). *Astrophys. J.* **364**, 672–686.

Weaver, H. A., P. D. Feldman, M. F. A'Hearn, C. Arpigny, J. C. Brandt, M. C. Festou, M. Haken, J. B. McPhate, S. A. Stern, and G. P. Tozzi 1997a. The activity and size of the nucleus of Comet Hale–Bopp (C/1995 O1). *Science* **275**, 1900–1904.

Weaver, H. A., T. Y. Brooke, G. Chin, S. J. Kim, D. Bockelée-Morvan, and J. K. Davies 1997b. Infrared spectroscopy of Comet Hale–Bopp. *Earth, Moon, Planets* **78**, 71–80.

Whipple, F. L. 1950. A comet model.I. The acceleration of Comet Encke. *Astrophys. J.* **111**, 375–394.

Xie, X., and M. J. Mumma 1996. Monte Carlo simulation of cometary atmospheres: Application to Comet P/Halley at the time of the Giotto spacecraft encounter. II. Axisymmetric model. *Astrophys. J.* **464**, 457–475.